Ko, V. and Teo, T.L.and Liew, T. and Chong, T.C. and MacKenzie, M. and MacLaren, I. and Chapman, J.N. (2008) *Origins of ferromagnetism in transition-metal doped Si.* Journal of Applied Physics, 104 . 033912. ISSN 0021-8979

http://eprints.gla.ac.uk/5953/

Deposited on: 9 June 2009

Origins of ferromagnetism in transition-metal doped Si

V. Ko
Graduate School for Integrative Sciences and Engineering, National University of Singapore, 28 Medical Drive, Singapore 117456

K.L. Teo[a], T. Liew and T.C. Chong
Information Storage Materials Laboratory, Electrical & Computer Engineering Department, National University of Singapore, 4 Engineering Drive 3, Singapore 117576 and Data Storage Institute, 5 Engineering Drive 1, Singapore 117608

M. MacKenzie, I. MacLaren, J. N. Chapman
Department of Physics and Astronomy, University of Glasgow, G12 8QQ, Scotland, UK

We present results of the magnetic, structural and chemical characterizations of Mn^+-implanted Si displaying *n*-type semiconducting behavior and ferromagnetic ordering with Curie temperature, T_C well above room temperature. The temperature-dependent magnetization measured by superconducting quantum device interference (SQUID) from 5 K to 800 K was characterized by three different critical temperatures (T_C^* ~ 45 K, T_{C1} ~ 630-650 K and T_{C2} ~ 805 - 825 K). Their origins were investigated using dynamic secondary mass ion spectroscopy (SIMS) and transmission electron microscopy (TEM) techniques, including electron energy loss spectroscopy (EELS), Z-contrast STEM (scanning TEM) imaging and electron diffraction. We provided direct evidences of the presence of a small amount of Fe and Cr impurities which were unintentionally doped into the samples together with the Mn^+ ions, as well as the formation of Mn-rich precipitates embedded in a Mn-poor matrix. The observed T_C^* is attributed to the Mn_4Si_7 precipitates identified by electron diffraction. Possible origins of T_{C1} and T_{C2} are also discussed. Our findings raise

---

[a] Electronic mail: eleteokl@nus.edu.sg

questions regarding the origin of the high Tc ferromagnetism reported in many material systems without a careful chemical analysis.

Keywords: Spintronics, Ferromagnetic semiconductors, Manganese, Silicon

I. INTRODUCTION

The electron spin arising from electrons in ferromagnets is the basis of the multi-billion dollar magnetic data-storage industry. The use of the spin-degree of freedom, in addition to the charge, in nanoelectronic devices holds great potential for devices with new functionality, high switching speed, low power consumption, non-volatility, high device density and the opportunity to converge microelectronics and magnetic technologies. However, many ferromagnets are not compatible with current microelectronic materials. Owing to the long range ferromagnetism (FM) as well as semiconducting properties exhibited by ferromagnetic semiconductors (FMS), they are promising candidates as a compatible source of spin-polarized carriers for spin injection into the semiconductor to realize nanoscale semiconductor spintronics devices.[1,2,3] In this aspect, Si-based FMS, with high Curie temperature, T_C, which can easily be integrated into the current semiconductor technology are highly desirable. Great efforts have been made in developing Group-IV FMS such as Mn-doped Ge, but they are considered far away from being a high-T_C FMS.[4,5] The major challenges are to obtain a pure FMS with $T_C > 500$ K, well above device operating temperature, and to understand the origins of FM in FMS. Ferromagnetism with $T_C > 400$ K has been reported in $Mn_{0.05}Si_{0.95}$ films fabricated through sputtering deposition[6] as well as in Mn^+ ion-implanted Si.[7,8] No magnetization measurement beyond 400 K has been reported in the Mn_xSi_{1-x} system so far, and little is known

about its structural properties. Despite theoretical calculations[9,10,11,12,13] predicting FM in transition-metal (TM) doped Si and recent transmission electron microscopy (TEM) studies on the low-T_C Mn_xSi_{1-x},[14] the origin of FM in this system is still not well understood.

It is now commonly known that samples containing single-phase random alloys, clusters of magnetic atoms, secondary phases and TM impurities which can contribute to the observed magnetic behavior can readily be produced depending on the growth conditions selected.[15] The last named in particular is often neglected or claimed to be absent when characterization with inadequate detection sensitivity is carried out on FMS. The implication is that detailed structural and chemical characterization, including nanoscale analysis, is needed to provide fresh insight into the possible mechanisms for the observed FM.

In this article, we report the magnetic properties of Si doped with TM using ion-implantation. We pay special attention to the chemical and structural analysis of precipitates observed in the material and their correlation with the magnetic properties. Owing to its ability to obtain both chemical and structural information on the nanoscale, we employ a range of analytical TEM techniques to investigate the origins of the FM in this system.

II. EXPERIMENTAL DETAILS

Ion-implantation was used to synthesize Mn_xSi_{1-x}. In addition to enabling quick synthesis of FMS, implantation is suitable for applications because selected contact regions for spin-polarized carrier injection can be formed in device structures. Undoped-Si (001) wafers were implanted with Mn^+ ions with purity of 99.9 % at a constant energy of 200 keV and with two different dosages of 1.0×10^{16} and

2×10^{16} cm^{-2}, labeled as S1 and S2, respectively. Samples were held at 350 ºC during implantation and then subjected to furnace annealing at 900 ºC for 10 min for re-crystallization. Magnetic properties were investigated using a commercial superconducting quantum interference device (SQUID) magnetometer with an in-plane applied magnetic field. Samples were cooled from 390 K for field-cooled (FC) and zero-field cooled (ZFC) magnetization measurements. An oven was used for high-temperature (400 to 800 K) SQUID measurement. We have excluded any possible contribution from the sample holder in the oven sample space or other spurious effects in the SQUID measurements. One approach we took is by performing the magnetic measurement without a sample to determine the contribution from the sample holder. The diamagnetic background from the Si substrate has been subtracted from the measurements.

The electrical properties of the samples were measured at room temperature in a van der Pauw configuration. Chemical compositions and depth profiles were obtained by X-ray photoelectron spectroscopy (XPS) and dynamic secondary ions mass spectroscopy (SIMS). Microstructural and further chemical analyses of the samples were carried out using TEM. Cross-sectional TEM specimens were prepared by gluing two pieces of wafer face-to-face followed by standard grinding, polishing and dimpling methods. Final thinning was achieved by Ar ion milling in a Gatan precision ion polishing system (PIPS). Most of the TEM investigations were performed in an FEI Tecnai F20 TEM/STEM equipped with a field emission gun, a Gatan ENFINA electron spectrometer and an EDAX X-ray spectrometer. Electron energy loss spectroscopy (EELS) spectrum imaging was performed using Gatan DigiScan and Digital Micrograph software. An FEI Tecnai T20 equipped with a CCD camera was used for convergent beam electron diffraction.

III. STRUCTURAL AND CHEMICAL ANALYSIS

Figure 1 presents the SIMS depth profiles of S1 and S2. The SIMS chemical analysis revealed the presence of unexpected Fe and Cr impurities besides the implanted Mn, although neither was detected by our XPS, Rutherford backscattering (RBS) and extended X-ray absorption fine structure (EXAFS) measurements. The Fe and Cr profiles follow that of the implanted Mn and their peak positions coincide with each other. In other words, the Fe and Cr elements were present as doping impurities during the Mn ion implantation process. The source of such impurities is not clear. Nevertheless, in what follows we have to take account of the real composition of the samples.

The Mn distributions show double peaks for both S1 and S2. These are associated with the segregation of implanted Mn^+ ion as recrystallization fronts move through the implanted layer during annealing.[16,17] This suggests that the impurities are trapped at specific defective regions such as vacancy-rich or interstitial-rich regions. Some of the impurities are segregated to the surface. The main peak of the Mn profiles is located at a depth of ~ 170 nm and the corresponding absolute Mn concentrations for S1 and S2 are 1.92×10^{20} (0.4 at. %) and 8.94×10^{20} (1.8 at. %) atoms/cm^3, respectively. The Fe and Cr peak concentrations are measured to be 1.77×10^{19} and 4.05×10^{18} atoms/cm^3, respectively for S1, and the corresponding values for S2 being 2.87×10^{19} and 7.03×10^{18} atoms/cm^3. The atomic concentration of Fe in the implanted Si sample is thus less than 0.06 at. %, and it is much lower for Cr. Therefore, we hereafter discuss our results by treating the samples as Mn and Fe co-implanted Si, albeit the Fe is present at a much lower concentration. Our X-ray

diffraction (XRD) data shows no evidence of secondary phase formation that would influence the magnetic properties of these samples within its detection limit.

The TEM studies showed that Mn-containing precipitates had formed in samples S1 and S2. Figure 2(a)-(b) shows high angle annular dark field (HAADF) STEM images of samples S1 and S2 in cross-section. As the HAADF images are dominated by Z-contrast, the precipitates which contain Mn, a heavier element than Si, appear bright and the glue lines between the two pieces of wafer appear dark. The majority of them are located in a subsurface band, i.e. between 150 to 350 nm from the surface, consistent with the SIMS data. As well as having more precipitates than S1, S2 also contains larger precipitates. The upper limit for the size of the precipitates observed in S1 was ~ 37 nm, whereas in S2, several precipitates with size as large as ~ 46 nm were observed. At these sizes, it would be reasonable to assume the precipitates exhibit bulk properties if they are magnetic. Some small particles of W (as determined by EDX) right at the surface of both sides of the glue line can also be observed in the HAADF images; the origin of these is unclear but they should not affect the magnetic properties of the samples. The precipitates can also be observed in the corresponding bright field STEM images (see Fig. 2(c) and (d)) but here the presence of strong diffraction contrast makes them more difficult to see. Defects in the form of dislocations can be seen to be associated with the sample surface and the precipitate rich bands. The formation of the precipitates could be caused by supersaturation and diffusion of Mn atoms during substrate heating as well as post-implant annealing. This is especially true because Mn interstitials are fast diffusers in Si,[18] and their diffusion increases when implanted regions contain numerous defects as observed here. In the HRTEM images as shown in Fig. 3, the precipitates appear either approximately spherical or ellipsoidal in shape; it should be noted that the

ellipsoidal precipitates viewed end on would appear spherical. Both shapes are present in both samples and both shapes show some evidence of faceting. The appearance of lattice and moiré fringes in these HRTEM images confirms that the precipitates are crystalline.

Convergent beam electron diffraction was performed to investigate the crystallographic structure of randomly chosen precipitates. Two examples are shown in Fig. 4 from two different precipitates in S2. Figure 4(a) shows a [210] diffraction pattern clearly showing periodicities related to the long c-axis of the Mn_4Si_7 structure, accompanied by a simulation. The strong 001 spots will arise through double diffraction from {124} and {123} planes. Figure 4(b) shows a [443] diffraction pattern colored in yellow, which is also characteristic of the Mn_4Si_7 structure. The weak 110 diffraction spots arise through double diffraction and are indicated on the simulation in grey. The simulations were obtained using Desktop Microscopist (Virtual Laboratories). The diffraction patterns of several other precipitates were indexed and also showed good matches with Mn_4Si_7 as did selected area diffraction patterns. Fast Fourier transforms (FFTs) of HRTEM images from some of the precipitates also indexed as Mn_4Si_7. Thus, we conclude that many of the precipitates are of the tetragonal Mn_4Si_7 phase.[19]

The chemical composition of the precipitates was investigated using EDX and EELS. The EDX analyses confirmed that the precipitates contained Mn as seen in Fig. 5. The EELS was performed in the form of point analyses, and both 1D and 2D spectrum imaging showing the presence of O, Cr and Fe as well as Mn in the precipitate containing regions. The oxygen was present in the form of surface oxidation which had occurred in thin regions of the TEM specimen and did not appear to be related to the precipitates. Figure 6 contains data from a 2D EELS spectrum

image from S1. Figure 6(a) is a HAADF image showing the precipitate from which the dataset was acquired and Fig. 6(b) shows the ADF signal acquired simultaneously with the spectrum image along with the Mn, Fe, Cr and O elemental maps created from the spectrum image. The O K-edge is from surface oxidation but the Cr, Mn and Fe $L_{2,3}$-edges are related to the precipitate although the Cr level is low. Figure 6(c) shows the summed spectrum over the precipitate region showing the relative heights of the Cr, Mn and Fe peaks. Sample S2 also showed Fe to be present in some of the precipitates but the Cr was observed in the form of blobs which were smaller and appeared brighter than the precipitates in the HAADF STEM images. Many of these Cr blobs were isolated from precipitates and while some looked at first sight to be cores within the precipitates, it is possibly just a result of the image projection effect in TEM. Figure 7 shows a HAADF STEM image of such a precipitate in S2 and the corresponding EELS point analyses with the background subtracted under the Cr edges. The Cr signal is clearly related to the bright blob. This can also be seen in the data from an elliptical precipitate in Fig. 8. Based on Fig. 8(b), the Mn and Fe signals track the precipitate, the Cr is localised to the bright blob and the O shows no correlation with the precipitate.

From the results presented above and others not shown here, we conclude that the Fe signal appears to be associated with Mn precipitates in both S1 and S2 although the level is non-uniform, varying from precipitate to precipitate. To date, we have not observed any Fe in Mn-free or Mn-poor regions. On the other hand, the presence of Cr does not always correspond to the presence of Mn.

Detecting the presence of Si in small precipitates of differing sizes embedded in a Si matrix is non-trivial. However, EELS has an advantage. Since the core-loss EELS probes the local density of unoccupied states and as such it is sensitive to

differences in the local chemical environment. Figure 9 shows the change in the near edge fine structure on the Si L-edges between the matrix and the precipitate region, confirming that there is Si present in another chemical environment than the matrix. In order to quantify the Mn:Si ratio in the precipitates, it is necessary to ensure that there is no remaining matrix surrounding the precipitate or to use advanced fitting techniques[20] to separate out the different Si contributions. Attempts were made to quantify the composition of precipitates on the thin edge of the TEM sample where the matrix had been thinned away by the TEM specimen preparation. However, these attempts were hindered by the lack of an experimental reference standard. Also it was found that the composition obtained was very sensitive to the theoretical cross-section model and the energy windows used. Using 50 eV energy windows and hydrogenic cross-sections with white line corrections, compositions consistent with the precipitates being Mn_4Si_7 were obtained. Figure 10 shows the compositional profile deduced from EELS across a precipitate on one of the thin edges of S2 sample.

No evidence of Mn was found in the matrix adjoining the precipitate containing regions or near the surface in either sample. However, we cannot rule out the existence of Mn of concentration ≤ 1 at. % within the matrix, as this is below the detection limit of the TEM investigations. Mn is known to segregate at precipitate matrix interfaces[21,22] but detection of low levels of Mn in the immediate vicinity of a Mn-rich precipitate is hampered by probe tails and specimen drift occurring during the relatively long acquisition times needed to achieve the requisite signal to noise. As such the possibility of Mn-enrichment in the matrix, immediately in the vicinity of the precipitates cannot be completely eliminated.

IV. MAGNETIC AND ELECTRICAL PROPERTIES

Hysteresis (*M-H*) loops measured at 300 K before the samples were annealed indicated that some ferromagnetic ordering existed around room temperature in as-implanted samples. After annealing, the magnetization increased by about a factor of three, from 0.15 to 0.50 emu/cm^3 for S2. The low value of magnetization in the samples may be due to the presence of antiferromagnetic coupling between the Mn moments and an appreciable number of magnetically inactive Mn atoms. Figure 11(a) shows the *M-H* curves at 300 K for the annealed S1 and S2 samples. A hysteresis loop is observed, S2 having a higher magnetization as expected due to its higher Mn concentration. The coercive field, H_c and the saturation field, H_s at 300 K for both samples were measured to be ~ 100 Oe and ~ 2.0 kOe, respectively. The H_c decreases with increasing temperature; from 200 Oe to 85 Oe when the temperature is raised from 5 K to 380 K. The ZFC-FC curves measured at 100 Oe for S1 and S2 are shown in the inset of Fig. 11(a). We clearly observe the T_C persists up to 390 K. A divergence between the ZFC and FC curves at low temperatures as well as reversibility above 350 K are observed. The ZFC curves have a weak maximum at above 150 K and are rather smooth and flat at high temperatures. The ZFC curves reach a maximum at ~ 170 K and ~ 310 K for S1 and S2, respectively. Although this behavior deviates from the ideal superparamagnetic system, it is consistent with the existence of a distribution of precipitate sizes and/or interaction among them in the samples, and with S2 containing precipitates of larger sizes than S1.

Figure 11(b) shows the temperature-dependent magnetization curves measured from 410 to 800 K for S1 and S2. The magnetizations are found to persist up to even 800 K for both the samples. The magnetization curves show a distinct change in slope near 600 K and 750 K. These are indicative of the existence of two different ferromagnetic phases, or regions with different composition within the sample. Two

transition temperatures are obtained by fitting with an empirical Brillouin function,

$M_s (T) = M_0 [1-(T/T_c)^2]^{1/2}$. For S1, $T_{C1} \sim 630$ K and $T_{C2} \sim 805$ K whilst for S2,

$T_{C1} \sim 650$ K and $T_{C2} \sim 825$ K. The origin of these transition temperatures will be

discussed in the next section.

Figure 12(a) shows the ZFC-FC curves of S2 at different applied fields. The

temperatures at which the ZFC and FC curve diverge, decrease with increasing

applied field. The shape of the FC curve below 300 K is more of a concave type,

which deviates from the mean-field theory, as given by the Brillouin function. This

could be the combined effect of spin disorder and low carrier density in this

system.[23,24] It is clearly seen that the low temperature curve becomes more outwardly

concave with increasing field. This can be explained by the increasing number of the

impurities or clusters being spin polarized by the external magnetic field. Additionally,

we observe a peak at $T_C^* \sim 45$ K in both the ZFC and FC curves which becomes more

pronounced at higher field. The appearance of this narrow peak is attributed to the

Mn_4Si_7 phase with a $T_C^* \sim 47$ K; a phase known to be present from section III. The

strong increase of magnetization at ~ 45 K at higher magnetic field is caused by the

higher fraction of magnetic moments of the Mn_4Si_7 clusters aligning along the

external magnetic direction. Such a change in magnetic order induced by sweeping

the magnetic field is called a metamagnetic transition and has been observed in

Mn_4Si_7 previously.[19]

Figure 12(b) shows the combined *M-T* data of the high temperature range (400

K to 800K) and the low temperature range (5 K to 390 K) for S2. These data are

overlaid together with the remanent magnetization, M_r data measured from 5 K to 350

K. The M_r data was collected during warm up in zero external field, after cooling

down from 350 K in 2 kOe. As for the M_s data, an external field of 1 kOe was applied during cooling down and warming up. As seen from both the curves, the low temperature magnetizations overlap with each other and show a deviation from mean-field-like behavior. We have fitted the M_r data with a second order exponential decay function and the function fits exceedingly well to the M_r data over the whole temperature range. A critical temperature at $\sim$ 670 K is obtained when extrapolated to a zero value. This is in good agreement with the T_{c1} value obtained from the M_s-T plot. Therefore, we considered the $T_{C1} \sim$ 650 - 670 K as the long range ferromagnetic transition temperature of this system. In the presence of applied field, the measurable magnetization extends up to 800 K, and thus indicates the existence of another distinct phase with $T_{C2} \sim$ 825 K.

The Mn$^+$-implanted Si displays a semiconducting or insulating electrical behavior. The resistivities measured at room temperature for S1 and S2 are $\approx$ 1.4×10^{-1} and $\approx 2.4 \times 10^{-1}$ Ω.cm, respectively. In contrast to the ferromagnetic Mn-doped Ge which is known to be p-type, Mn$^+$-implanted Si is measured to be an n-type semiconductor. It is known that the energy levels induced by TM doping into Si are deep in the energy gap. For example, donor levels in between 0.42 eV to 0.55 eV have been reported in Mn and Fe doped Si samples.[25,26] Therefore, the implanted impurities in our samples serve as donors and the deep levels are thought to be located on the upper sides of the energy gap. Interstitial atoms and crystal defects may also introduce unwanted electronic states that can lead to compensation or n-type conduction. This indicates that the mechanism of the high-T_C ferromagnetism in our samples is unlikely to be hole-mediated. The carrier concentrations at room temperature for S1 and S2 are measured and estimated to be around 1.6×10^{18} and

1.3×10^{17} cm^{-3}, respectively. The much lower carrier concentration in S2 compared to S1 can be attributed to the higher densities of defects and precipitates formed as observed from the STEM images shown in Fig. 2, which results in the loss of electrical activated dopants. The carrier densities are found to be below the critical density, $N_{crit.}$ for metal-insulator-transition (MIT) in Si, as the Mott criterion yields a critical concentration of $N_{crit.} \sim 3.5 \times 10^{18}$ cm^{-3} by assuming an effective Bohr radius of $a_B = 15$ Å.[27] Therefore, our systems are on the insulating side of MIT and the carriers are considered to be localized, which is consistent with the observed shape of the M-T curves.

V. DISCUSSIONS OF THE FERROMAGNETIC PROPERTIES

Based on the various results on FMS reported in the recent years, origins of ferromagnetism in FMSs can now be possibly explained by: (i) precipitation of secondary phase, (ii) spinodal nanodecomposition, (iii) Zener model of carrier mediated ferromagnetism, and (iv) bound magnetic percolation. Identification of the origin of FM is not a simple and straightforward problem. Nevertheless, we try to provide possible explanations on the origins of the ferromagnetism in this system based on our findings.

Firstly, we consider the magnetic properties of possible precipitates that can account for the ferromagnetism. The observation of a phase with $T_C^* \sim 45$ K fits well with the Mn$_4$Si$_7$ precipitates detected by TEM. On the other hand, Mn$_4$Si$_7$ has a $T_C \approx$ 47 K and so this cannot account for our observed FM at $T_C > 400$ K. Using TEM and SIMS, we also detected the presence of Fe and Cr impurities in our samples. Cr is antiferromagnetic and Cr silicides are paramagnetic, so the ferromagnetism cannot be

13

assigned to this source. However, a contribution from Fe cannot be excluded. Iron metallic clusters seem unlikely to be the cause as metallic Fe, at least in bulk form, has a high T_C ~ 1043 K. Since Fe was observed to track the Mn closely based on the elemental mapping, it seems likely that some mixed metal silicides formed where the metallic component was of the form $Mn_{1-x}Fe_xSi$ with $x < 0.1$. The upper limit to the value of x comes from our observation that even in S1, where most Fe was found; the EELS results suggested a Mn/Fe ratio ~ 11. One possible origin could be due to the formation of $Mn_{1-x}Fe_xSi$, but this phase cannot account for our magnetic results since this compound supports a helimagnetic phase with T_C below 50 K.[28] Another more hopeful possibility is that precipitates of cubic Fe_3Si may have formed and this compound being ferromagnetic with T_C reported as 823-839 K.[29] This is very close to the T_{C2} ~ 805 - 825 K obtained for our samples. However, we must stress that we have no direct evidence for the formation of such a phase from our TEM analysis.

A high-T_C spinodally nanodecomposed phase, as already reported in a variety of FMS systems and claimed in Ref. [30] to be a generic property of FMS, could offer an explanation of the obsserved T_{C1} value. Spinodal decomposition occurs when a single phase at high temperature transforms into two low-temperature phases with the same crystal structure but different composition and lattice parameters. It is induced by virtue of the instability of the system to a local composition gradient at a certain temperature. *Ab initio* calculations[31,32] have revealed a particularly strong tendency of FMS to form the decomposed phase magnetic network which gives rise to high-T_C values. Moreover, spinodal decomposition has been shown to lead to a high T_C in $(Ga,Mn)As$,[33,34] $(Zn,Cr)Te$,[30,35] $(Ga,Mn)N$,[36] $(Al,Cr)N$, $(Ga, Cr)N$[37], $(Ga,Fe)N$, [38]

(Ge,Mn)[39,40,41] and (Zn,Co)O.[42] Based on the random phase approximation[31], the T_C of (Ga,Mn)N could reach ~ 700 K with a Mn concentration of 30 %. Therefore, we tentatively suggest that the high T_C of our system, with its highly inhomogeneous Mn distribution based on clusters containing ~ 36 % Mn [See Fig. 10(c)], has a similar origin. Although our TEM analysis showed that the majority of precipitates were Mn_4Si_7, the spinodally decomposed Mn-rich phase could exist in a minority of precipitates or even as coherent phase not readily detectable in the matrix. The higher M_s and T_C of S2 as compared to S1 can be associated with the larger size and higher Mn content of the clusters, instead of higher carrier density as expected in the mean-field theory.

Although the magnetic properties of our system may be affected by Mn_4Si_7 precipitates and to a lesser extent from unintentional impurities such as Fe, carrier-mediated ferromagnetism, either within the matrix or the precipitates, cannot be excluded. If we assume it is the matrix rather than the precipitates that are important, we can infer on the effect of Mn in Si at a concentration < 1% and thus undetectable using the techniques we employed. Unfortunately there is a large discrepancy between our results and the Zener model of hole-mediated ferromagnetism. The model predicts a T_C ~ 150 K for Mn-doped Si containing 5 % of Mn and 3.5×10^{20} holes/cm^3.[43] Moreover, since the ferromagnetism of our samples is observed in the absence of free holes, the framework of standard models adopted in $Ga_{1-x}Mn_xAs$ and the mean field theory, is inapplicable. Hence an alternative to the Zener model was seek to explain our observed FM. Carriers localized on impurities forming bound magnetic polarons (BMP) with ferromagnetic coupling were considered as a possibility. This seemed plausible given (i) the insulating nature, (ii) the low carrier density (below N_{crit}), (iii)

15

the low saturation magnetization, (iv) the non-mean-field-like outwardly concave *M-T* curve, and (v) the presence of Mn-rich regions observed in our samples. Nevertheless, this seems to be a weak explanation of the high-T_C FM since the BMP model being more relevant to explaining magnetic behavior at low temperatures.

It is important to point out here that, unlike III-V DMS where antiferromagnetic pairing prevails when Mn impurities form complexes, it has been shown by first principle calculation in Ref. [10] that interstitial-interstitial and substitutional-interstitial defects in Mn-doped Si couple ferromagnetically. According to Ref. [44], isolated Mn impurities are known to exist with charge states from 1- to 2+ for the interstitial impurity, while for the subsitutional impurity the only charge state detected are 1+ and 2-. As for the Mn dimers, they are mostly neutral defects and have low formation energy. Therefore, the formation of Mn dimers such as the pairing of substitutional and interstitial Mn (Mn_S-Mn_I) is highly probable. Interstitials are likely to be present within the Mn^+-implanted Si samples along with the Mn_4Si_7 precipitates. Therefore, the high temperature ferromagnetic phase with $T_{C1} \sim 630$ - 650 K can tentatively be attributed to spinodally decomposed TM-rich clusters containing Mn (and Fe), which could also possibly contain dimers that ferromagnetically couple locally in the precipitates.

VI. CONCLUSIONS

In summary, ferromagnetism was observed in annealed Mn, Fe co-implanted Si(100) samples with three transition temperatures, $T_C^* \sim 45$ K, $T_{C1} \sim 630$ - 650 K and $T_{C2} \sim 805$ - 825 K being recorded. These puzzling T_C can be explained by three different magnetic phases: Mn_4Si_7 precipitates, Mn-rich nanophase, and an Fe-related

phase, respectively. Our studies illustrate the importance of careful correlation of the measured magnetic properties with high spatial resolution and elementally-sensitive analysis techniques. Indeed, our work raises questions about the origin of high-T_C ferromagnetism reported in many FMS where chemical profiles or impurity analysis by SIMS or EELS was not undertaken. Although spinodal decomposed Mn-rich nanophase and Fe related compounds can account for a high $T_C > 600$ K, we emphasize that this does not preclude the existence of carrier-mediated ferromagnetism in a systems with strongly localized carriers such as that investigated here, in particular within the Mn-poor matrix. The new insight gained here should assist in the development of superior materials for future Si-based spintronics applications.

FIGURE CAPTIONS

FIG. 1: SIMS chemical depth profiles of the annealed (a) S1 and (b) S2.

FIG. 2: (a)-(b) HAADF STEM images showing 2 pieces of S1 and S2 glued together in cross-section, respectively. Note that the glue lines run down the field of view and appear black while the precipitates appear bright and are found in a sub-surface precipitate-rich band; (c)–(d) the corresponding bright field STEM images in which dislocations can be seen at the sample surface and in the precipitate rich region.

FIG. 3: HRTEM images of precipitates in (a) S1 and (b) S2. Both shapes of precipitates were observed in both samples.

FIG. 4: (a) [210] CBED pattern from a Mn_4Si_7 precipitate in S2 and the corresponding simulation; (b) [443] CBED pattern from a Mn_4Si_7 precipitate in S2 and the corresponding simulation (in the experimental pattern spots from the Si matrix appear blue, and those from the precipitate are yellow).

FIG. 5: (a) HAADF STEM image of precipitates in S2; (b)-(c) are the EDX spectra obtained by scanning the beam in the regions indicated by the boxes on (a).

FIG. 6: (a) HAADF STEM image of precipitates in S1. The white box indicates the region from which an EELS spectrum image was acquired; (b) ADF signal acquired simultaneously with the spectrum image; Mn, Cr, Fe and O maps obtained from the EELS spectrum image; (c) Background subtracted EELS spectrum summed over the precipitate.

FIG. 7: (a) HAADF STEM image of precipitates in S2; (b) EELS spectra from the regions marked by the coloured boxes in (a).

FIG. 8: (a) HAADF STEM image of precipitates in S2. The white box indicates the region from which an EELS spectrum image was acquired; (b) ADF signal acquired simultaneously with the spectrum image; Si, Mn, Cr, Fe and O maps obtained from

the EELS spectrum image; (c) Background subtracted EELS spectrum summed over the Cr-rich region.

FIG. 9: (a) HAADF STEM image of precipitates in S2; (b) EELS Si L-edges obtained from the regions indicated by the boxes on (a).

FIG. 10: (a) HAADF STEM image of precipitates in S2 where the ion milling has removed most of the surrounding matrix. The white line indicates the region from which an EELS spectrum image was acquired; (b) ADF signal acquired simultaneously with the spectrum image; (c) Relative composition of Mn and Si across the precipitate.

FIG. 11: (a) M-H curves at 300 K for S1 and S2. The inset shows their ZFC (open circles)-FC(filled circles) curves from 5 K to 390 K under an applied field of 100 Oe; (b) M-T curves from 410 K to 800 K for S1 and S2 samples under an applied field of 1.5 kOe. The red dashed lines are fits to M_s (T) $=$ M_0 $[$ $1-($ T/T_c $)^2$ $]^{1/2}$.

FIG. 12: (a) ZFC (filled circles)-FC (open circles) curves for S2 from 5 K to 390 K at different applied fields; (b) normalized M_s/M_{5K} and M_r vs temperature for S2 from 5 K to 800 K. The red dashed lines are fit to M_s (T) $=$ M_0 $[$ $1-($ T/T_c $)^2$ $]^{1/2}$. The dashed green line represents the qualitatively expected remanence by second order exponential decay fit.
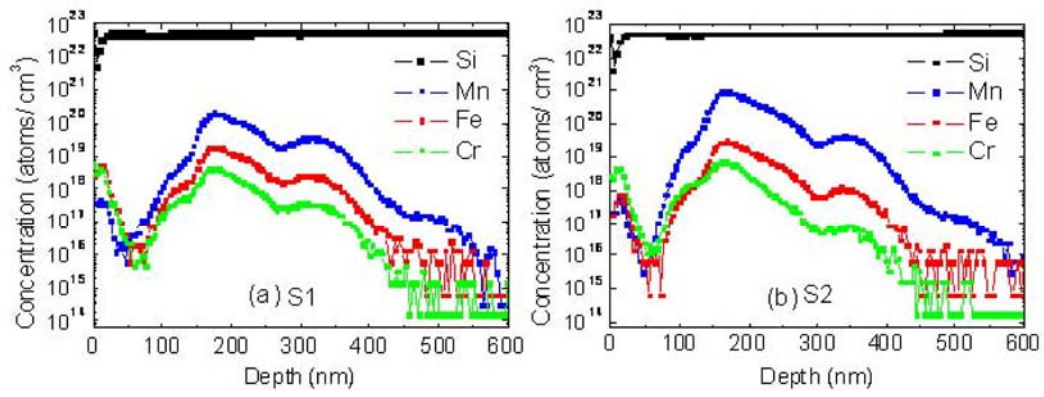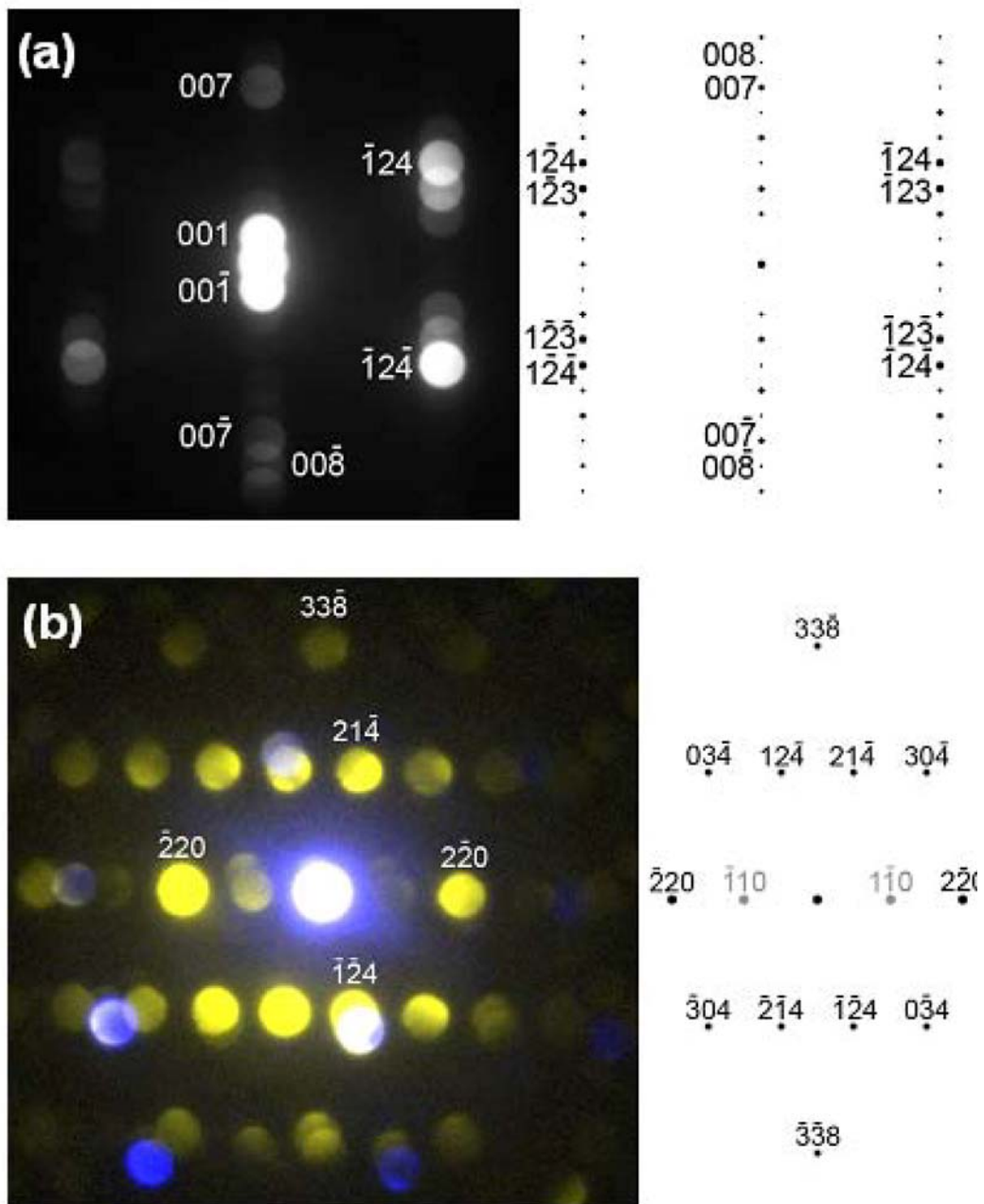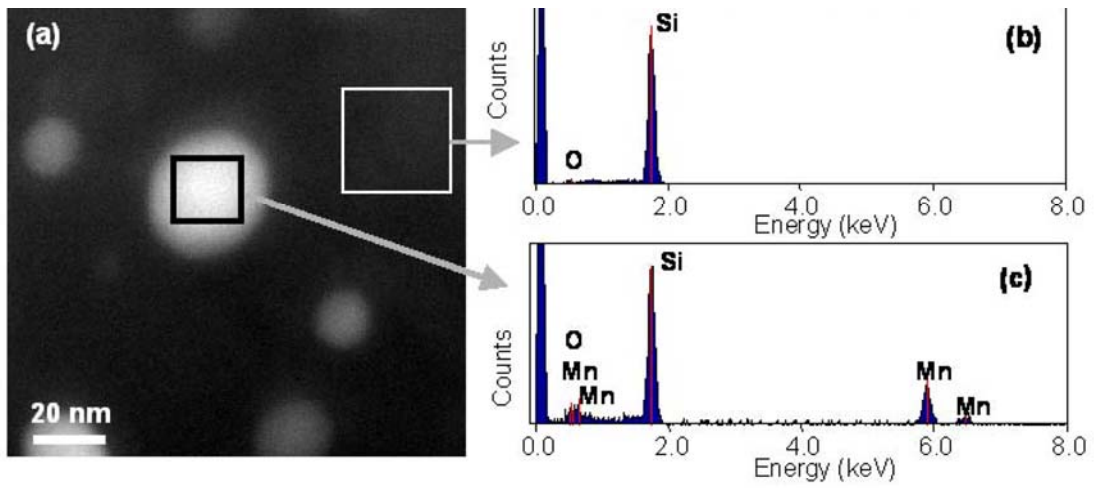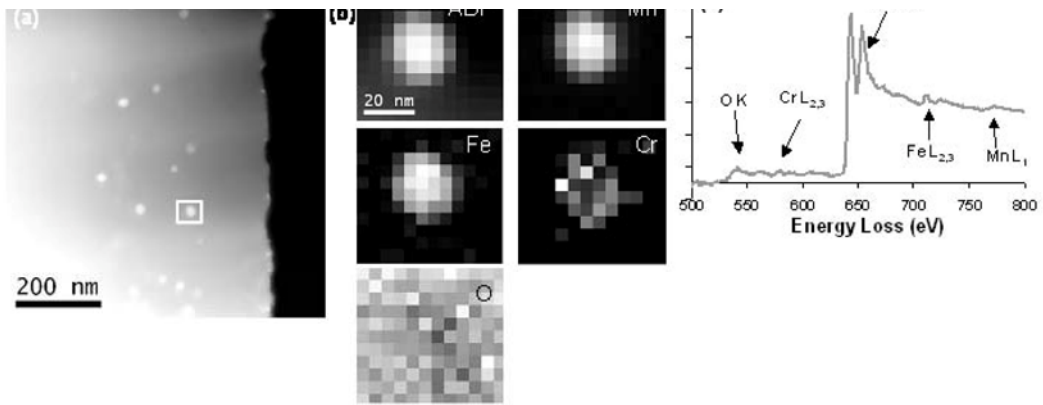
Fig. 1
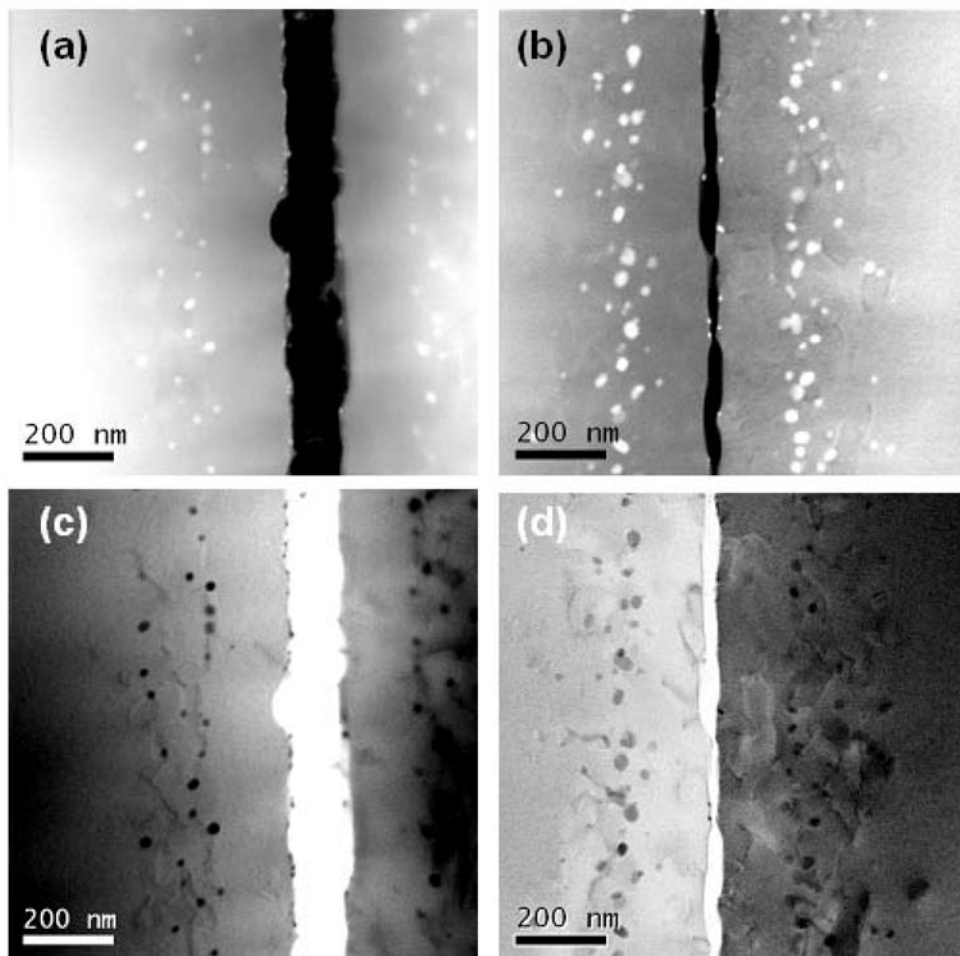
Fig. 2
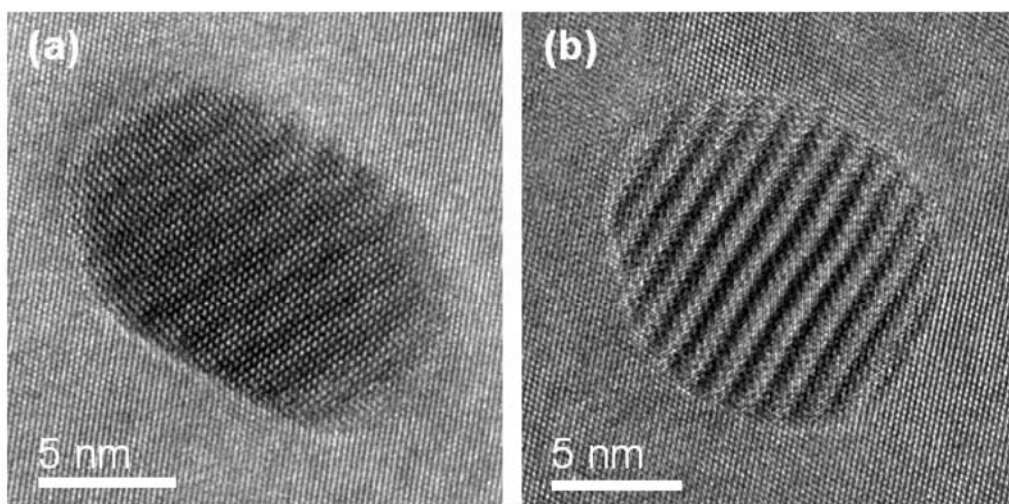
Fig. 3

Fig. 4

Fig. 5

Fig. 6
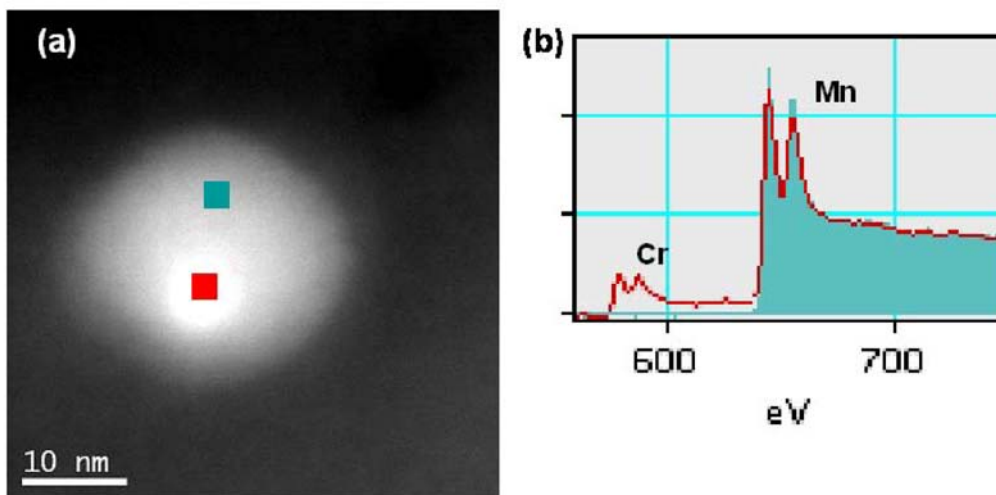
Fig. 7
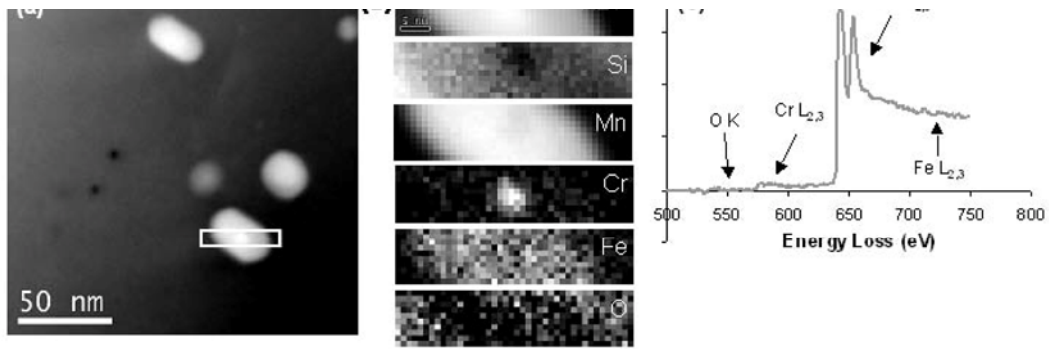
Fig. 8
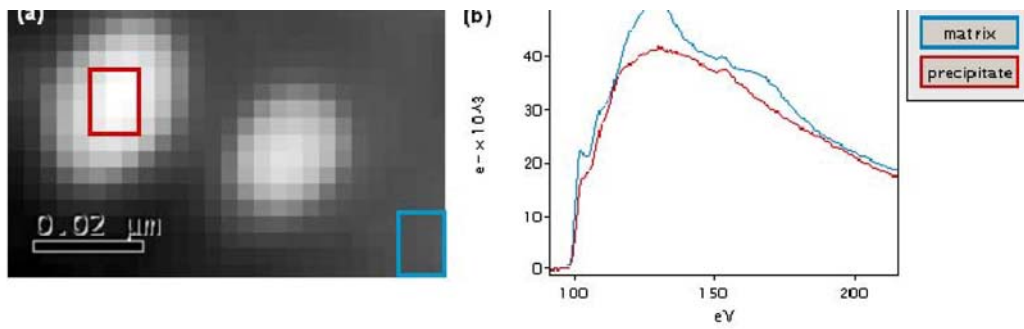
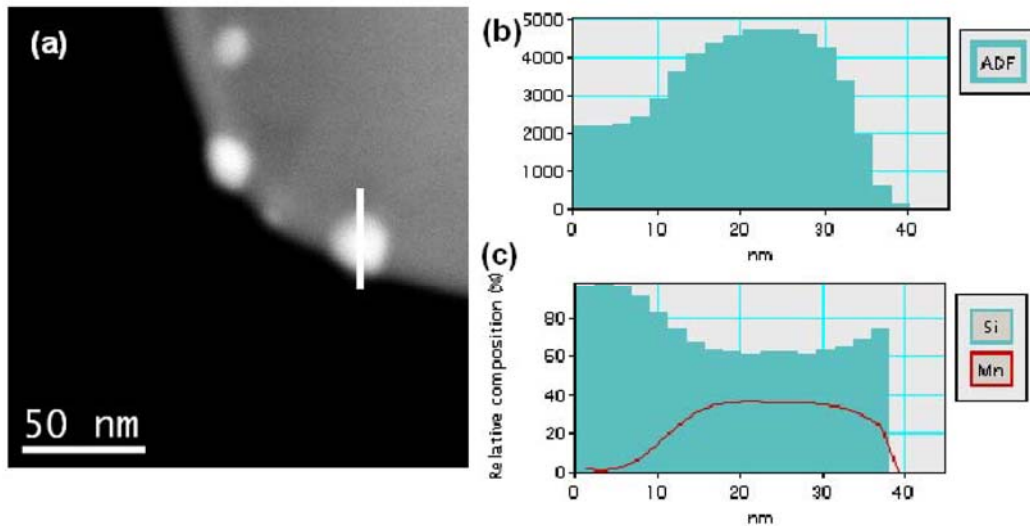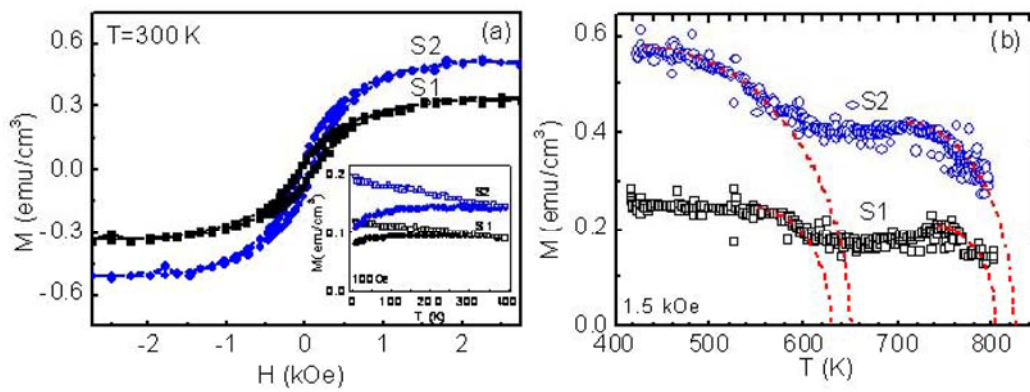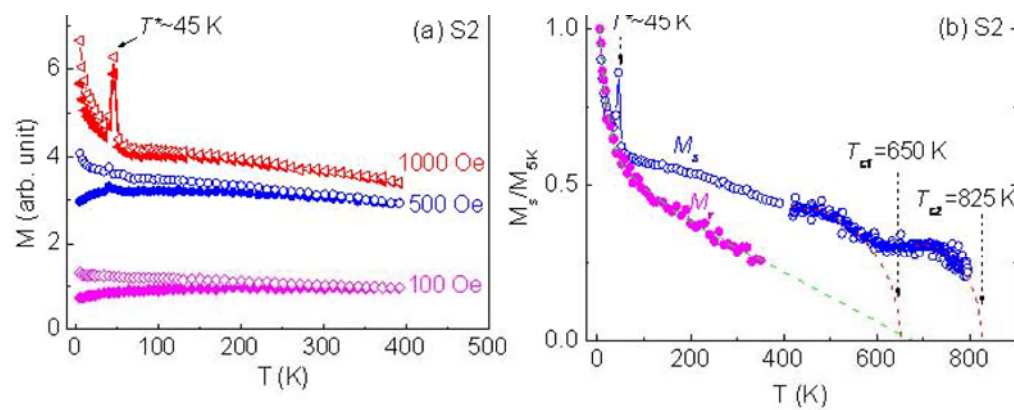**Fig. 9**

Fig. 10

Fig. 11

Fig. 12

REFERENCES

[1] S. Wolf, D. D. Awschalom, R. A. Buhrman, J. M. Daughton, S. von Molnar, M. L. Roukes, A. Y. Chtchelkanova and D. M. Treger, *Science* **294**, 1488 (2001).

[2] H. Ohno, F. Matsukura and Y. Ohno, *Jpn. Soc. Appl. Phys. Int.* **4**, 4 (2002).

[3] H. Akinaga and H. Ohno, *IEEE Trans. Nanotech.* **1**, 19 (2002).

[4] Y. D. Park, A. T. Hanbicki, S. C. Erwin, C. S. Hellberg, J. M. Sullivan, J. E. Mattson, T. F. Ambrose, A. Wilson, G. Spanos and B. T. Jonker, *Science* **295**, 651 (2002).

[5] A. P. Li, J. F. Wendelken, J. Shen, L. C. Feldman, J. R. Thompson, and H. H. Weitering, *Phys. Rev. B* **72**, 195205 (2005).

[6] F. M. Zhang, X. C. Liu, J. Gao, X. S. Wu, and Y. W. Du, *Appl. Phys. Lett.* **85**, 786 (2004).

[7] S. M. Bolduc, C. Awo-Affouda, A. Stollenwerk, M.B. Huang, F.G. Ramos, G. Agnello and V.P. LaBella, *Phys. Rev. B* **71**, 033302 (2005).

[8] H. W. Wu, C. J. Tsai, and L. J. Chen, *Appl. Phys. Lett.* **90**, 043121 (2007).

[9] A. Stroppa, S. Picozzi, A. Continenza, and A. J. Freeman, *Phys. Rev. B* **68**, 155203 (2003).

[10] F. Bernardini, S. Picozzi, and A. Continenza, *Appl. Phys. Lett.* **84**, 2289 (2004).

[11] Wu. H, M. Hortamani, P. Kratzer, and M. Scheffler, *Phys. Rev. Lett.* **92**, 237202 (2004).

[12] H. Weng, H. J. Dong, *Phys. Rev. B* **71**, 035201 (2005).

[13] H. Wu, P. Kratzer, and M. Scheffler, *Phys. Rev. Lett.* **98**, 117202 (2007).

[14] S. Zhou, K. Potzger, G. Zhang, A. Mucklich, F. Eichhorn, N. Schell, R. Grotzshel, B. Schmidt, W. Skroupa, M. Helm, and J. Fassbender, *Phys. Rev. B* **75**, 085203 (2007).

[15] T. Dietl and H. Ohno, *Materials Today* **9**, 18 (2006).

[16] D. K. Sadana, M. H. Norcott, R.G. Wilson, and U. Dahmen, Appl. Phys. Lett **49**, 1169 (1986).

[17] R. G. Wilson, D.M. Jamba, D. K. Sadana, and C. G. Hopkins, J. Appl. Phys. **61**, 1355 (1987).

[18] E. R. Weber, *Appl. Phys. A: Solids Surf.* **A30**, 1 (1983).

[19] U. Gottlieb, A. Sulpice, B. Lambert-Andron and O. Laborde, *J. Alloys Compounds.* **361**:13 (2003).

[20] M. MacKenzie, and A. J. Craven, J. Phys. D.: Appl. Phys., **33**, 1647 (2000)

[21] D. Isheim, M. S. Gagliano, M. E. Fine and D. N. Seidman, *Acta Mat.*, **54**, 841 (2006)

[22] S. Lozano-Perez, G. Sha, J. M. Titchmarsh, M. L. Jenkins, S. Hirosawa, A. Cerezo, and G. D. W. Smith: *J. Mater. Sci.*, **41**, 2559 (2006)

[23] M. Berciu and R. N. Bhatt, *Phys. Rev. Lett.* **87**, 107203 (2001).

[24] A. Kaminski and S. Das Sarma, *Phys. Rev. Lett.* **88**, 247202 (2002).

[25] W. Schroeter and M. Seibt, *Properties of Crystalline Silicon (EMIS Datareview Series No 20)* ed R. Hull, New York: INSPEC IEE, 561 (1999).

[26] C. B. Collins and R. O. Carlson, *Phys. Rev. B* **108**, 1409 (1957).

[27] Peter P. Edwards and Michell J. Sienko, *Phys. Rev. B* **17**, 2575 (1978).

[28] N. Manyala, Y. Sidis, J. F. DiTusa, G. Aeppli, D. P. Young, and Z. Fisk, *Nat. Mater.* **3**, 255 (2004).

[29] Landolt Bornstein III, *Magnetic Properties of Metals, Group III*, ed. H. P. J. Wijn, Springer-Verlag Berlin Heidelberg, Vol. **19c**, 26 and 101 (1988).

[30] S. Kuroda, N. Nishizawa, K. Takita, M. Mitome, Y. Bando, K. Osuch, and T. Dietl, *Nat. Mater.* **6**, 440-446 (2007).

[31] K. Sato, H. Katayama-Yoshida and Peter H. Dederichs, *Jpn. J. Appl. Phys.* **44**, L948 (2005).

[32] H. Katayama-Yoshida, K. Sato, T. Fukushima, M. Toyoda, H. Kizaki, V. A. Dinh, and P. H. Dederichs, *Phys. Stat. Sol.* **A204**, 15 (2007).

[33] M. Moreno, A. Trampert, B. Jenichen, L. Däweritz, and K. H. Ploog, *J. Appl. Phys.* **92**, 4672 (2002).

[34] M. Yokoyama, H. Yamaguchi, T. Ogawa, and M. Tanaka, *J. Appl. Phys.* **97**, 10D317 (2005).

[35] L. Gu, S. Wu, H. Liu, R. Singh, N. Newman, and D. Smith, *J. Magn. Magn. Mater.* **290–291**, 1395 (2005).

[36] G. MartineZ-Criado, A. Somogyi, S. Ramos, J. Campo, R. Tucoulou, M. Salome, J. Susini, M. Hermann, M. Eickhoff, and M. Stutzmann, *Appl. Phys. Lett.* **86**, 131927 (2005).

[37] L. Gu, S. Wu, H. Liu, R. Singh, N. Newman, and D. Smith, *J. Magn. Magn. Mater.* **290–291**, 1395 (2005).

[38] A. Bonanni, M. Kiecana, C. Simbrunner, T. Li, M. Sawicki, M. Wegscheider, M. Quast, H. Przybylińska, A. Navarro–Quezada, R. Jakieła, A. Wolos, W. Jantsch, and T. Dietl, *Phys. Rev. B* **75**, 125210 (2007).

[39] M. Jamet, A. Barski, T. Devillers, V. Poydenot, R. Dujardin, P. Bayle-Guillemaud, J. Rothman, E. Bellet-Amalric, A. Marty, J. Cibert, R. Mattana, and S. Tatarenko,

Nat. Mater. **5**, 653 (2006).

[40] D. Bougeard, S. Ahlers, A. Trampert, , N. Sircar and G. Abstreiter, *Phys. Rev. Lett.* **97**, 237202 (2006).

[41] J.-S. Kang, G. Kim, S. C. Wi, S. S. Lee, S. Choi, Sunglae Cho, S. W. Han, K. H. Kim, H. J. Song, H. J. Shin, A. Sekiyama, S. Kasai, S. Suga, and B. I. Min, Phys. Rev. Lett. **94**, 147202 (2005).

[42] T. Dietl, T. Andrearczyk, A. Lipińska, M. Kiecana, M. Tay, and Y. Wu, *Phys. Rev. B* **76**, 155312 (2007).

[43] T. Dietl, H. Ohno, F. Matsukura, J. Cibert and D. Ferrand, *Science* **287**, 1019 (2000).

[44] J. Kreissl, W. Gehlhoff, and H. Volmer, *Phys. Rev. B* **49**, 10307 (1994).